small structures
www.small-structures.com

Transport Property Evolution in 2H-$MoTe_{2-x}$ Mediated by Te-Deficiency-Induced Mirror Twin Boundary Networks

*Yinuo Zhang, Xueyan Li, Yuang Li, Di Wu, Xuecen Miao, Lan Li, Tai Min, and Yi Pan**

The 2H-$MoTe_2$ is a well-known layered 2D semiconductor that is considered as a promising material for next-generation microelectronic and optoelectronic devices. Te-deficiency-induced defective structures, like Te vacancy and mirror twin boundary (MTB), would be generated at elevated temperatures. However, the temperature-dependent evolution of such defects and their influence on the macroscopic electrical transport property of 2H-$MoTe_2$ is unclear. Herein, the semiconductor–metal transition phenomenon in 2H-$MoTe_{2-x}$ mediated by the evolving disordered MTB network with increasing Te deficiency is reported on. The samples are grown by molecular beam epitaxy, while the Te deficiency is tuned by post-growth flash annealing in ultra-high vacuum. Low-temperature scanning tunneling microscope investigation discloses the medium-range disorder evolution of the MTB network incorporated in the 2H-$MoTe_2$, which eventually transforms to an ordered metallic Mo_5Te_8 metastable phase. The scanning tunneling spectroscopy shows rich in-gap states localized at the MTBs, which provide a conducting channel in the semiconductor. The ultra-high vacuum in situ transport measurement shows a gradual decrease of resistance of the sample upon flash annealing from 50 to 480 °C, confirming the influence of Te deficiency on the transport property, which would play an essential role in the device performance and durability.

1. Introduction

As a two-dimensional (2D) layered material in the transition metal dichalcogenides (TMDCs) family, $MoTe_2$ has attracted increasing research interest in recent years due to its intriguing physical properties, as well as its promising applications in electronic and optoelectronic devices.[1–10] Its rich phase diagram features hexagonal (2H), distorted octahedral (1T′), and orthorhombic (T_d) phases, which endow $MoTe_2$ rich electronic properties such as semiconducting, semimetallic, ferroelectric, and superconducting characteristics.[3,4,9,11] The semiconducting 2H-$MoTe_2$ has been widely used as a tunable ambipolar channel material in different types of 2D transistors.[1,2,8,10–13] Like other 2H phase TMDCs, the 2H-$MoTe_2$ with Te deficiency (2H-$MoTe_{2-x}$) often contains various types of defects, including isolated Te vacancies and interconnected line defects, which are either formed during growth or generated afterward due to chalcogen desorption or excess metal deposition.[14–23] The line defects often appear as networks of bright double lines, already observed on the van der Waals epitaxial grown $MoSe_2$ in the early scanning tunneling microscope (STM) studies,[24,25] but were misinterpreted as distortion caused by lattice mismatch. Later, the atomic structure of the double line was established as a mirror twin boundary (MTB) with metallic in-gap states based on high-resolution transmission electron microscope and STM characterizations.[26]

The origin of these networks in $MoSe_2$ was found to be Se deficiency during growth or induced by electron beam irradiation.[17] Such chalcogen-deficiency-related MTB has been found in many other TMDC materials, like MoS_2, $MoTe_2$, WS_2, and WSe_2.[27–29] Due to the one-dimensional (1D) confinement of the domain boundary with nanometer width, the metallic in-gap states localized at the MTB show strong correlation effects, evidenced by the charge density wave (CDW).[30–32] Thus, the MTB network embedded in the semiconducting body is predicted to have a dramatical influence on the transport property of the system via enhancing the conductivity,[33] as well as introducing 1D quantum transport behavior,[26] which are yet to be explored in defect-dependent transport measurements.

Apart from inducing local electronic states, the randomly distributed single defects and inhomogeneous MTB network would also bring about medium-range disorder in the lattice.[34] Although the MTB sometimes forms a quasiperiodic wagon-wheel structure with varying periodicity from a few to dozens of nanometers, the ordering of such superstructure is never strict in the long range.[19,35,36] At the atomic structure level, the chemical bonds within the trigonal prismatically coordinated 3Te–Mo–3Te building block remain the same, but the blocks at the twin boundary are incomplete due to the loss of 2 Te atoms in

Y. Zhang, X. Li, Y. Li, D. Wu, X. Miao, L. Li, T. Min, Y. Pan
Center for Spintronics and Quantum Systems
State Key Laboratory for Mechanical Behavior of Materials
Xi'an Jiaotong University
Xi'an 710049, China
E-mail: yi.pan@xjtu.edu.cn

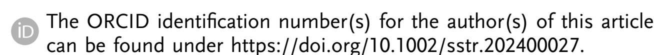
The ORCID identification number(s) for the author(s) of this article can be found under https://doi.org/10.1002/sstr.202400027.

© 2024 The Authors. Small Structures published by Wiley-VCH GmbH. This is an open access article under the terms of the Creative Commons Attribution License, which permits use, distribution and reproduction in any medium, provided the original work is properly cited.

DOI: 10.1002/sstr.202400027

each block. In this way, the periodicity of the crystal lattice is interrupted by the shift of the Te sublattice perpendicular to the MTB. The medium- and long-range disorder within 2D lattice has been studied in many 2D materials, like amorphous graphene, vitreous monolayer silica, and some amorphous 2D TMDCs.[37–41] Additionally, it was found that the disorder in 2D materials could give rise to some intriguing electronic properties,[41] for example, the metal–insulator transition of 10^9 times resistance increase in monolayer graphene tuned by atomic-scale structure disorder.[37] Recently, it has been reported that higher Te deficiency in $MoTe_2$ would eventually lead to a metallic Mo_5Te_8 phase,[42] in which the ordering was perfectly restored, and flat-band related exotic electronic states were proposed.[43]

On the other hand, the macroscopic transport performance of 2D semiconductors in advanced electronic devices is susceptible to the local structure and electronic structure of the 2D materials owing to their natural atomic-scale thickness and nanoscale line width of the device. The atomic defects in 2H-$MoTe_2$, i.e., Te vacancy, would play an essential role in the new device functions, like atomic-level memristors.[44,45] They are also crucial factors accounting for the device performance and thermal stability, sometimes dominated by the defects-related structures.[46,47] In this sense, a causal link between atomic-scale disorder and macroscopic transport properties is highly demanded. Nevertheless, the systematic investigation of the Te-deficiency-dependent structure ordering evolution and corresponding electronic structure transition in 2H-$MoTe_{2-x}$ largely remains elusive so far. In particular, an atomic-level understanding of the influence of the MTB on the macroscopic conductivity is still lacking.

In this work, we report a combined atomic-scale local structure and macroscopic transport study on epitaxial 2H-$MoTe_2$ thin films by utilizing an ultra-high vacuum (UHV) STM and a home-built in situ transport measurement setup at varying vacuum annealing temperatures. The evolution of Te-deficient defects upon increasing post-growth annealing temperatures was elucidated by high-resolution STM images. The influence of evolving defects on the medium-range order of the lattice was investigated by performing Fourier transform and radial distribution function analysis on the simulated intermediate structures based on STM topographic images. The local density of states arising from different types of defects was revealed by scanning tunneling spectroscopy (STS). To evaluate the macroscopic transport properties of corresponding samples while avoiding disturbing factors like oxidation and phase transition, the conductivity was investigated by measuring the current–voltage (I–V) relationship in the UHV environment immediately after each annealing step. These results disclose thermal annealing induced the semiconductor–metal transition phenomenon in 2H-$MoTe_2$, originating from the evolution of disordered MTB networks.

2. Results and Discussion

2.1. Synthesis of 2H-$MoTe_{2-x}$ with Tunable Te Deficiency

The 2H-$MoTe_{2-x}$ films were grown on highly oriented pyrolytic graphite (HOPG) or GaN(0001) substrates by the molecular beam epitaxy (MBE) method, as shown in the schematic diagram of the sample preparation strategy in **Figure 1**a–c. The growth parameters and setups are described in the method section and our previous work.[48] The atomically resolved STM image confirmed the formation of crystalline 2H-$MoTe_2$ on the HOPG, as shown in Figure 1d. The fine-tuning of Te-deficiency defects, mainly vacancies and MTBs, is realized by post-growth flash vacuum annealing followed by abrupt cooling, as illustrated in Figure 1b,c. Since Te desorption at elevated temperatures is a fast process, in the typical tens of minutes time-scale annealing and natural cooling process, the density of Te vacancy cannot be easily controlled. We adopt the flash annealing and abrupt cooling strategy to obtain the snapshots of transient Te-deficient structures, as sketched in Figure 1b. A series of samples containing varying densities of Te vacancies and MTBs were successfully synthesized, as shown in the STM images in Figure S1, Supporting Information. A representative image is displayed in Figure 1e, in which the MTB network can be clearly observed. These experimental results are essential for the statistical analysis and simulation of MTB evolution in $MoTe_{2-x}$. Eventually, the Te vacancy approaches a saturation with moderated high-temperature annealing at ≈350 °C, as demonstrated in Figure 1c. The metastable crystalline Mo_5Te_8 phase was formed then, as shown in the STM image in Figure 1f. These results confirmed that our strategy is effective for fine-tuning Te deficiency in 2H-$MoTe_{2-x}$, which then felicitated the further investigation of MTB evolution and structure ordering.

Based on the series of high-resolution STM images with increasing Te deficiency, the evolution of Te vacancy defects and MTB in the 2H-$MoTe_{2-x}$ could be depicted in the following scenario. Upon vacuum annealing at around 150 °C, isolated Te vacancies appear, as shown in Figure S1b, Supporting Information, because of Te desorption from the lattice. When the vacancy density increases at higher annealing temperatures, the vacancies would line up and form MTB (see Figure S1b, Supporting Information), similar to the emergence of MTBs in $MoSe_2$ and $MoTe_2$ induced by local electron beam irradiation.[19,35] With increasing length, the MTBs tend to form closed triangles with a critical side length rather than further extend linearly, most likely due to the accumulating strain energy in one direction. Upon further increasing vacancy density at higher annealing temperatures, the isolated MTB triangles would form a network, as shown in Figure 1e and S1c, Supporting Information. As the triangles in the network are not uniform in size, the medium-range (from a few to dozens of nanometers) disordering emerges in the 2D lattice. The MTB network becomes denser and more disordered at even higher annealing temperature, as shown in Figure S1d, Supporting Information. However, the evolution of 2D 2H-$MoTe_{2-x}$ eventually stopped at a crystalline $MoTe_{1.6}$ (i.e., Mo_5Te_8) structure, which is a metastable phase recently reported in the samples prepared in a similar method.[42]

By conducting the statistical analysis of the series of high-resolution STM images, the average Te/Mo ratio curve versus the density of MTB was calculated, as plotted in Figure 1g. The calculation detail is described in the Supporting Information. The blue diamond, red squares and pinky triangle indicate the crystalline 2H-$MoTe_2$, $MoTe_{2-x}$ with disordered MTB and the crystalline Mo_5Te_8, respectively. The dashed line connecting

© 2024 The Authors. Small Structures published by Wiley-VCH GmbH

26884062, 2024, 7, Downloaded from https://onlinelibrary.wiley.com/doi/10.1002/sstr.202400027 by Xian Jiaotong University, Wiley Online Library on [19/12/2024]. See the Terms and Conditions (https://onlinelibrary.wiley.com/terms-and-conditions) on Wiley Online Library for rules of use; OA articles are governed by the applicable Creative Commons License

26884062, 2024, 7, Downloaded from https://onlinelibrary.wiley.com/doi/10.1002/sstr.202400027 by Xian Jiaotong University, Wiley Online Library on [19/12/2024]. See the Terms and Conditions (https://onlinelibrary.wiley.com/terms-and-conditions) on Wiley Online Library for rules of use; OA articles are governed by the applicable Creative Commons License

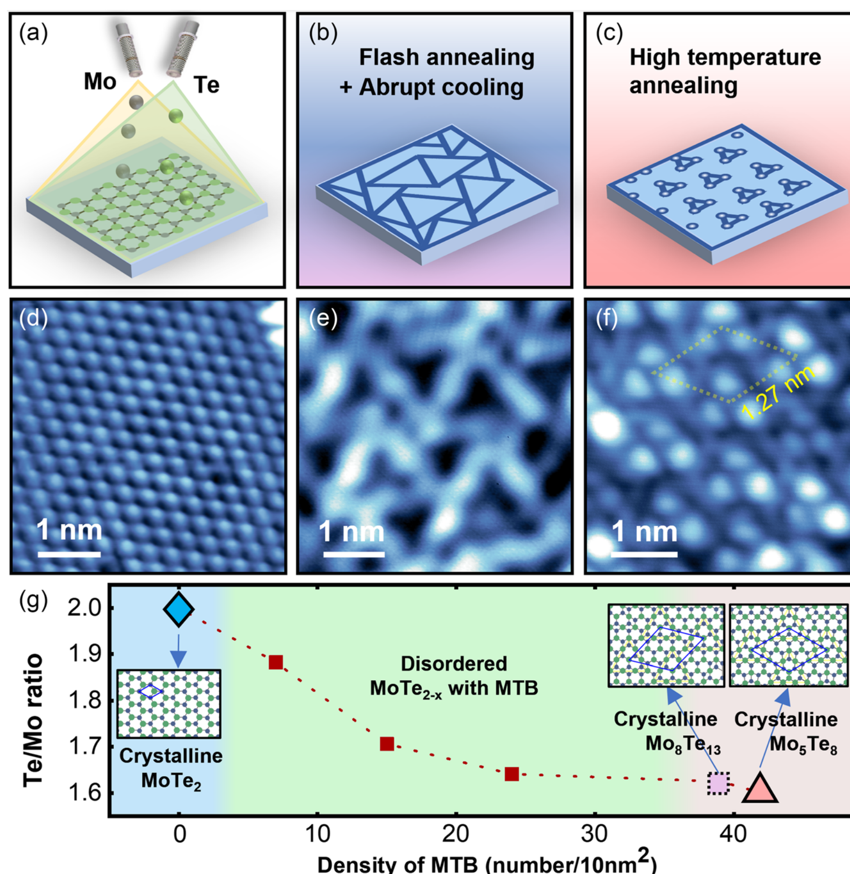

Figure 1. Synthesis of 2H-$MoTe_{2-x}$ with gradually increasing Te deficiency by MBE growth and postannealing in UHV. a–c) Schematic diagrams of the sample preparation strategy: (a) crystalline stoichiometric 2H-$MoTe_2$ by codeposition of Mo and Te; (b) 2H-$MoTe_{2-x}$ with disordered MTB network by flash annealing and abrupt cooling; (c) crystalline Mo_5Te_8 by high-temperature annealing. d–f) the representative STM topographic images corresponding to (a–c), respectively. The tunneling parameters: (d) $V_b = -1.4$ V, $I_t = 100$ pA; (e) $V_b = 2.0$ V, $I_t = 100$ pA; (f) $V_b = 20$ mV, $I_t = 50$ pA. g) The average Te/Mo ratio is deduced from the density of MTB (number of MTB unit cells in every 10 nm^2) in the STM data, showing the structure evolution. The blue diamond, red squares and pinky triangle indicate the crystalline 2H-$MoTe_2$, $MoTe_{2-x}$ with disordered MTB and the crystalline Mo_5Te_8, respectively. The dashed pinky square indicates a crystalline Mo_8Te_{13} phase, which was not observed in the experiments.

these points clearly shows the structure evolution trend, which reveals the presence of a disordered state of the 2D film between the crystalline 2H-$MoTe_2$ and Mo_5Te_8 phases. In principle, the densest MTB network preserving the bond angles of the 2H-$MoTe_2$ framework should be a crystalline Mo_8Te_{13} structure, as indicated by the dashed pinky square and displayed in the inserted model. However, such a crystalline phase was not observed in our experiment. We speculate that the Mo_5Te_8 structure is energetically more favorable due to the structure relaxation with bonding angle change.

2.2. Evolution of the Local Structure Disordering and Electronic Structure

The structure ordering of the 2H-$MoTe_{2-x}$ samples is investigated by analyzing the fast Fourier transformation (FFT) patterns acquired from the simulated ball-stick models, namely, the defect-free crystalline 2H-$MoTe_2$, the $MoTe_{2-x}$ with disordered MTB network, and the crystalline Mo_5Te_8. These structure models are constructed according to the high-resolution STM images, as demonstrated in **Figure 2**a–c and S2, Supporting Information. The corresponding FFT patterns are presented in Figure 2d–f, respectively. Figure 2d shows sharp spots in the clean and dark background, representing the perfect periodic lattice of the 2H-$MoTe_2$. The pattern in Figure 2e shows a notable increase of the background intensity, which confirms the emerging disorder in 2H-$MoTe_{2-x}$ with MTB network. The pattern in Figure 2f shows additional sharp spots with a dark background, revealing a periodic lattice with a superstructure that arises from the larger unit cell of Mo_5Te_8.

To compare the ordering of the three structures, the intensity profiles of the spots along the dashed yellow lines are plotted in Figure 2g–i. The noisy curve with a broad peak in Figure 2h clearly shows the presence of disorder in the highly defective lattice with an MTB network. Additionally, the radial distribution curves obtained by calculating the atom distribution from the center of the models are plotted in Figure 2j,k for crystalline 2H-$MoTe_2$ and $MoTe_{2-x}$ with a disordered MTB network, respectively. The multiple small peaks in Figure 2k confirm

 © 2024 The Authors. Small Structures published by Wiley-VCH GmbH

26884062, 2024, 7, Downloaded from https://onlinelibrary.wiley.com/doi/10.1002/sstr.202400027 by Xian Jiaotong University, Wiley Online Library on [19/12/2024]. See the Terms and Conditions (https://onlinelibrary.wiley.com/terms-and-conditions) on Wiley Online Library for rules of use; OA articles are governed by the applicable Creative Commons License

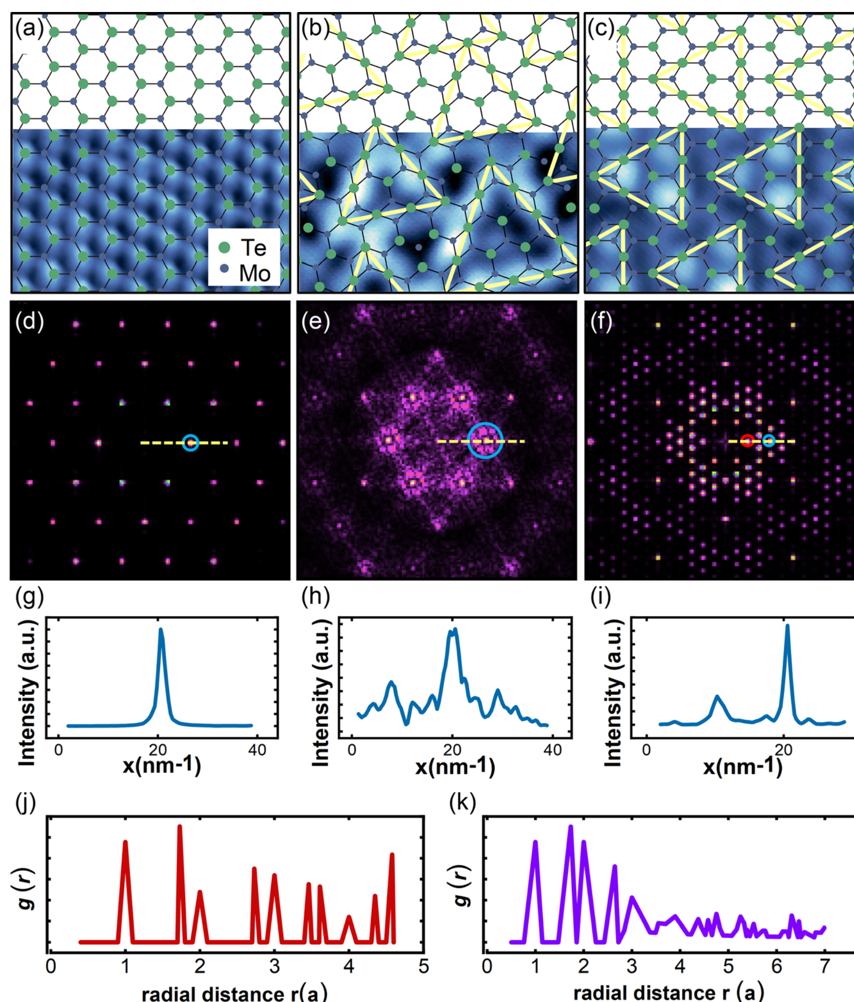

Figure 2. Structure ordering analysis of the 2H-$MoTe_{2-x}$. a–c) Ball-stick models of (a) defect-free crystalline 2H-$MoTe_2$, (b) $MoTe_{2-x}$ with disordered MTB network, and (c) crystalline Mo_5Te_8, superimposed on the STM images. d–f) FFT patterns of simulated structure models corresponding to panel (a–c). g–i) The line profile intensity of the low order spots indicated by the dashed yellow lines in the FFT patterns (d–f), respectively. j,k) The radial distribution curves obtained from the center of the models of crystalline 2H-$MoTe_2$ and $MoTe_{2-x}$ with disordered MTB network, respectively.

the medium-range disorder induced by MTBs. When the Mo:Te ratio approaches 5:8, the lattice ordering will be gradually recovered due to the formation of a new phase.

Figure 3a is a zoom-in STM topological image (with resolution change during scanning) of the $MoTe_{2-x}$ surface showing the detailed local structure of the MTB network. The normal resolution (lower part) and atomically high resolution (upper part) were recorded in the same image because of a random event of the tip apex change (marked by the yellow dashed line) while scanning from the lower to the upper part. In the lower part of the image, which is in normal resolution, the MTBs appear as lines of bright protrusions with a periodicity of 3 times the lattice constant along the boundary. Such modulation comes from the CDW arising at the quasi-1D MTB at low temperature.[30] The upper part shows the atomic resolution of the MTB. Interestingly, the resolution of the image was suddenly improved due to unintentional tip change, most likely by picking up an atom from the surface, as indicated by the dashed yellow line in Figure 3a. In the high-resolution image zoomed-in on the MTB (see Figure 3b), the boundary appears as four rows of atomic chains brighter than the pristine area, implying higher conductivity in the MTB. By comparing the STS taken on the MTB (marked by the black cross) with the pristine 2H-$MoTe_2$ region (marked by the red cross), it can be found that the MTB shows number of peaks (−397, −113, and 440 mV) in the bandgap of the 2H-$MoTe_2$, as displayed by the black and red curves in Figure 3c, respectively. Thus, the origin of the high conductivity in the MTB could be elucidated as the in-gap states. Such states are attributed to the *d* orbitals of Mo atoms and *p* orbitals of Te atoms at the boundary.[17,26] Additionally, we have acquired the STS spectrum on the Mo_5Te_8 samples, which shows multiple peaks with a small gap around the Fermi level rather than a large bandgap, implying better conductivity. These STM results depict the evolution trend of the local electronic structure, increasing in-gap states and shrinking bandgap with increasing Te deficiency, accompanied by the evolving disorder of the 2H-$MoTe_{2-x}$.

© 2024 The Authors. Small Structures published by Wiley-VCH GmbH

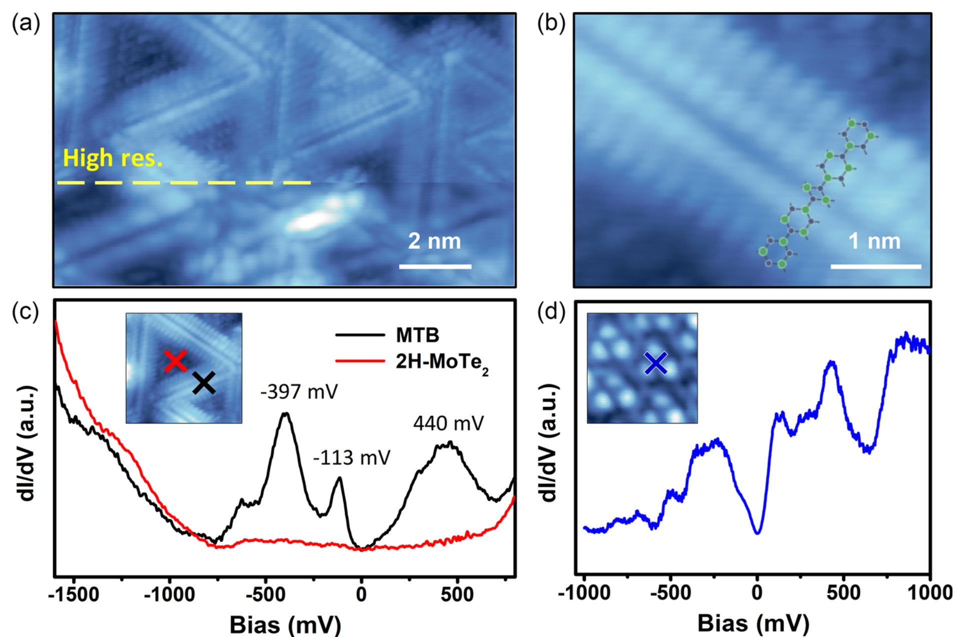

Figure 3. Local structure and electronic structure of the 2H-$MoTe_{2-x}$. a) STM image of the MTB network showing CDW patterns in normal resolution (lower part) and bright chains in high resolution (upper part). b) A ball-stick model of the MTB superimposed on the high-resolution image of the MTB obtained with a modified tip. c) STS spectra taken at the location indicated by the red and black crosses. The peaks in the black curve reveal the in-gap states arising at the MTB. d) STS spectrum acquired at the Mo_5Te_8 samples, which shows multiple peaks with a small gap around the Fermi level.

2.3. UHV Flash Annealing and In Situ Conductivity Measurement

The microscopic-scale understanding of the $MoTe_{2-x}$ inspires us to further investigate its macroscopic electrical transport properties influenced by the structure evolution with increasing Te deficiency. To avoid the interference of substrate conductivity, we change the substrate from HOPG to the wide-gap substrate GaN(0001). The 2H-$MoTe_2$ was grown on the GaN(0001) surface with the same growth method under the UHV condition. Then, patterned Au electrodes were immediately deposed on the $MoTe_2$ with the help of shadow mask. The photo of a typical device (upper panel) and the optical microscopic image of the film (lower panel) are shown in **Figure 4**a. We confirmed the as-grown $MoTe_2$ film is in 2H phase by examining its Raman spectrum, which has three characteristic peaks indicating the out-of-plane A_{1g} (≈173.3 cm^{-1}), in-plane E^1_{2g} (~234.8 cm^{-1}), and out-of-plane B^1_{2g} (≈290 cm^{-1}) vibration modes, as shown in Figure 4b. Such large-scale continuous films are suitable for the following electrical transport measurements.

To avoid the influence of oxidation, we designed an in situ transport experiment in a UHV chamber, as sketched in Figure 4c. The key point to realize this experiment is combining the flash annealing preparation and in situ transport measurement of the gradually increasing Te-deficient 2H-$MoTe_2$ samples. To that end, we modified a commercial flag-type MBE sample holder (see the photo in Figure 4d) by providing a conducting channel through two Ta plates to the Au electrodes on the sample. The reliable contact was realized by inserting gold foil between the Ta plate and deposited Au electrodes, as shown in the schematic diagram of the cross-sectional structure in Figure 4d. One of the Ta plates was grounded to the sample holder, while the other was isolated from the sample holder by a ceramic ring in between. The isolated Ta plate end was connected to the UHV feedthrough bar in the vacuum side via copper wire. Then, the feedthrough was connected to a Keithley 2400 source measure unit. By this way, the in situ I–V measurement could be conducted after each flash annealing when the sample was naturally cooled down to room temperature (RT, ≈30 °C). The reliability of this method is proved by the control experiments, as demonstrated in Figure S3, Supporting Information.

A series of flash annealing was conducted in the temperature range from RT to 480 °C. Each annealing step was followed by in situ I–V characterization at 30 (±2) °C. The representative I–V curves, obtained after 50 and 480 °C flash annealing, are plotted in Figure 4e in blue and red, respectively. The linear I–V curve confirmed the stable ohmic contact at the electrodes. The 50 °C annealing sample, which is actually degassed as a control specimen, shows a resistance of 5.3 (±1.2) × 10^7 Ω. In contrast, the 450 °C annealing sample shows a resistance of 0.91 (±0.07) × 10^5 Ω, which is much lower than the control specimen. The inserted panel in Figure 4e shows the same curve in logarithmic coordinates, which reveals that the 480 °C flash annealing gives rise to a dramatic conductivity increase by two orders of magnitude. Such a drastic change of resistance, which is carefully measured in UHV condition without the interference of chemical contamination, confirmed that the Te-deficient defects in 2H-$MoTe_2$ have strong influence on its transport property.

By performing statistical analysis, we obtained the sheet resistance (R_s) as a function of annealing temperature, as shown in Figure 4f. It reveals that the evolution of resistance could be

© 2024 The Authors. Small Structures published by Wiley-VCH GmbH

26884062, 2024, 7, Downloaded from https://onlinelibrary.wiley.com/doi/10.1002/sstr.202400027 by Xian Jiaotong University, Wiley Online Library on [19/12/2024]. See the Terms and Conditions (https://onlinelibrary.wiley.com/terms-and-conditions) on Wiley Online Library for rules of use; OA articles are governed by the applicable Creative Commons License

26884062, 2024, 7, Downloaded from https://onlinelibrary.wiley.com/doi/10.1002/sstr.202400027 by Xian Jiaotong University, Wiley Online Library on [19/12/2024]. See the Terms and Conditions (https://onlinelibrary.wiley.com/terms-and-conditions) on Wiley Online Library for rules of use; OA articles are governed by the applicable Creative Commons License

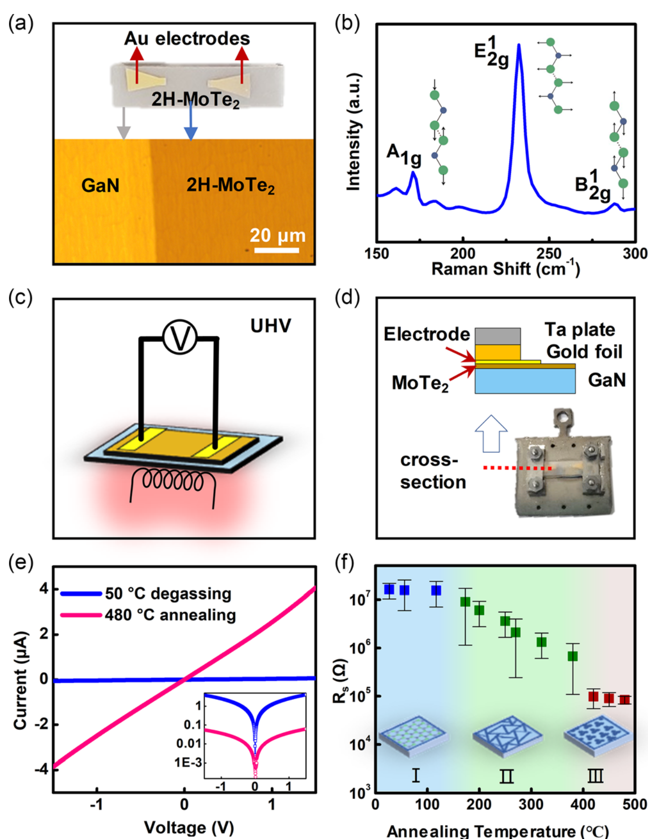

Figure 4. UHV flash annealing and in situ conductivity measurement of the $2H\text{-}MoTe_{2-x}$. a) Upper: photo of MBE epitaxial $2H\text{-}MoTe_2$ grown on GaN substrate with UHV deposited Au electrodes under a shadow mask. Lower: optical microscope image of the as-grown $2H\text{-}MoTe_2$. b) Raman spectrum taken on the as-grown film, with the main vibration modes indicated by the ball-stick models. c) Schematic diagram showing the design of the UHV in situ transportation measurement setup. d) The assembled sample on a flag type MBE sample holder for in situ transport measurement. The contact between the Au electrode and the Ta plate is demonstrated in the cross-sectional schematic diagram. e) The representative *I–V* curves obtained after 50 and 480 °C flash annealing. Insert: the same curves in logarithmic plot. f) Statistical results of conductance obtained after flash annealing at various temperatures, which reveal three stages in the evolution of the resistance, marked as I, II, and III.

divided into three stages (marked as I, II, and III), as indicated by the light blue, green, and red areas in Figure 4f. In stage I, there are no significant changes of the resistance when the annealing temperature is below ≈160 °C. We attribute the effect of low-temperature annealing to the outgassing of surface adsorbates and the formation of isolated Te vacancies, which does not affect the macroscopic electric property of the film. The measured resistance is at the level of $\approx 10^7\,\Omega$, consistent with the reported semiconductive properties of $2H\text{-}MoTe_2$.[49] In stage II, the resistance gradually decreases from $\approx 10^7$ to $\approx 10^5\,\Omega$, with the annealing temperature further raised to 160–390 °C, as shown in the green region in Figure 4f. Such a decrease of resistance could be attributed to the formation of vacancy chains and the growth of MTB networks. In previous studies, it has been speculated that the reduction of $MoTe_{2-x}$ resistivity might come from the chalcogen deficit-related defects,[33,50] but without direct microscopic observations. These MTBs would form a network that provide metallic channels in the 2D semiconductor layer. Due to the disorder in the material, the resistance deviation is also increased. In stage III, the resistance becomes stable while maintaining at the level of $10^5\,\Omega$, while the annealing temperature is elevated to 400–480 °C. This behavior could be explained as the crystalline Mo_5Te_8 phase is formed when the density of the MTBs reaches the maximum, which has been revealed by our STM results and previous works. The phase transition from $2H\text{-}MoTe_2$ to Mo_5Te_8 is mainly driven by Te desorption. We speculate the substrate interaction might also play a role in the formation of such a metastable phase. The details of the phase transition mechanism are still yet to be further explored.

These results suggest a microscopic electrical property transition from semiconducting to metallic behavior, which is better understood by the microscopic evolution of Te-deficiency defects, mainly the disordered MTB network, as is revealed by the STM observations. The crystalline-to-amorphous transformation accompanied by semiconductor-to-metal transition has been experimentally observed in ion irradiated MoS_2.[51] In particular, the MTB network induced metallization in MoS_2 was theoretically predicted by J. Park et al. based on comprehensive calculations.[50] The Te-deficiency defects-related conductance increment in $2H\text{-}MoTe_{2-x}$ was also noticed before.[33] Our results agree with these earlier works, and provide the causal link between atomic-scale structure defects and macroscopic transport property change.

For the practical application of 2D semiconductor-based devices, the influence of high temperature, either from the ambient environment or the heat generated by the device itself, would be a crucial factor to consider because it may cause device malfunction. Here, in the case of $2H\text{-}MoTe_2$-based field-effect transistor, the transition of electrical response from gate modulation to the degenerately p-doped (hole dominant) characteristics caused by high operation temperature has been observed.[52] One should pay more attention to the possible shortcut caused by the gradual development of MTB, which has a relatively low onset temperature threshold. On the other hand, introducing chalcogen defects like vacancy and MTB in the 2D semiconductors may find useful applications, such as enhanced chemical reactivity or novel quantum transport at low temperature.

3. Conclusion

In conclusion, we have investigated the microscopic structure evolution in $2H\text{-}MoTe_{2-x}$ and its influence on the macroscopic electrical transport property of the film. The samples are prepared by MBE method, and the Te deficiency in the samples were well tuned by UHV flash annealing and abrupt cooling on a liquid nitrogen cooled sample stage. The atomic-resolution STM images reveal that the MTB structure evolves with increasing Te deficiency, i.e., the average Te/Mo ratio varies from 2.0 to 1.6. Additionally, the FFT analysis reveals the medium-range lattice disorder caused by the randomly formed MTB networks. Eventually, a metastable Mo_5Te_8 phase is formed, and the crystallinity is restored. The STS spectrum reveals robust in-gap states (−397, −113, and 440 mV) associated with the MTB,

© 2024 The Authors. Small Structures published by Wiley-VCH GmbH

which would provide the conducting channels in the semiconducting 2H-$MoTe_2$. The UHV in situ electrical transport measurement, which was realized with a specially designed sample holder, confirmed that the resistance of 2H-$MoTe_{2-x}$ gradually drops from $5.3\ (\pm 1.2) \times 10^7\ \Omega$ to $0.91\ (\pm 0.07) \times 10^5\ \Omega$ with the flash annealing in the range from 160 to 390 °C, consistent with the evolution of MTB network. Finally, the film shows stable metallic-like behavior due to the formation of Mo_5Te_8. These results reveal that high-temperature-induced chalcogen deficiency, which is common in the TMDC, could have a significant influence on macroscopic transport properties. Our work also provides a valuable method to trace the link between atomic-scale structure and the macroscopic properties of low-dimensional materials.

4. Experimental Section

MBE Growth: Epitaxial $MoTe_2$ films were grown on HOPG substrate and GaN (Suzhou Nanowin Science and Technology Co., Ltd.) substrate in a UHV MBE system, which is equipped with quartz crystal microbalance for thickness controlling and reflection high-energy electron diffraction for quality monitoring of materials. The molybdenum and Te were codeposited on the heated HOPG substrate from electron beam and effusion cell evaporators, respectively. During growth, high-purity Mo (99.95%, Alfa Aesar) and Te (99.999%, Alfa Aesar) were coevaporated by standard K-cell and E-beam evaporator, respectively. The Te/Mo flux ratio was kept at 10:1 during the deposition while the substrate temperature was maintained at 340 °C.

Flash Annealing Method: Te-deficient structures were synthesized by flash annealing and abrupt cooling strategy. The flash annealing was realized by quickly raising the temperature to the target value and maintaining it for 3–5 s, and then abruptly cooled down the sample stage by filling liquid nitrogen. After that, the sample was immediately transferred to a custom-made cryogenic STM (Createc LT STM).

STM Measurement: STM measurement was performed at 77 K using an electrochemically etched W tip. The tunneling spectra were obtained by using lock-in technique with 5–20 mV AC modulation voltage at 833 Hz.

Transport Measurement: Commercial flag-shaped sample holder had been modified to ensure ohmic contact to the ultrathin film. The sample mounted on the holder were inserted in a home-made sample stage with contact pins wired to UHV feedthrough. The background vacuum in the chamber was maintained at $P < 10^{-6}$ Pa by a turbo molecular pump. The radiation heating plate (maximum power of 50 W) was mounted at backside of the sample holder with a distance of about 2 mm. The sample surface temperature was measured by a pyrometer (optris CSLaser LT) with the measurement range from −30 to 1000 °C and accuracy of ±0.3 °C. A source measure unit (Keithley 2400) was connected to the feedthrough for the *I–V* and resistance measurement.

Supporting Information

Supporting Information is available from the Wiley Online Library or from the author.

Acknowledgements

This work was financially support by the National Key Research and Development Program of China (grant no. 2022YFA1204100), the National Natural Science Foundation of China (grant no. 12074302), and the Fundamental Research Fundings for the Central Universities. The authors thank the Instrument Analysis Center of Xi'an Jiaotong University for their assistance with Raman spectra measurement.

Conflict of Interest

The authors declare no conflict of interest.

Data Availability Statement

The data that support the findings of this study are available from the corresponding author upon reasonable request.

Keywords

2H-$MoTe_2$, mirror twin boundary, semiconductor–metal transition

Received: January 19, 2024
Revised: March 10, 2024
Published online: April 12, 2024

[1] N. R. Pradhan, D. Rhodes, S. Feng, Y. Xin, S. Memaran, B.-H. Moon, H. Terrones, M. Terrones, L. Balicas, *ACS Nano* **2014**, *8*, 5911.
[2] S. Nakaharai, M. Yamamoto, K. Ueno, Y.-F. Lin, S.-L. Li, K. Tsukagoshi, *ACS Nano* **2015**, *9*, 5976.
[3] Y. Qi, P. G. Naumov, M. N. Ali, C. R. Rajamathi, W. Schnelle, O. Barkalov, M. Hanfland, S. C. Wu, C. Shekhar, Y. Sun, V. Suss, M. Schmidt, U. Schwarz, E. Pippel, P. Werner, R. Hillebrand, T. Forster, E. Kampert, S. Parkin, R. J. Cava, C. Felser, B. Yan, S. A. Medvedev, *Nat. Commun.* **2016**, *7*, 11038.
[4] J. Chen, G. Wang, Y. Tang, H. Tian, J. Xu, X. Dai, H. Xu, J. Jia, W. Ho, M. Xie, *ACS Nano* **2017**, *11*, 3282.
[5] Y. Wang, J. Xiao, H. Zhu, Y. Li, Y. Alsaid, K. Y. Fong, Y. Zhou, S. Wang, W. Shi, Y. Wang, A. Zettl, E. J. Reed, X. Zhang, *Nature* **2017**, *550*, 487.
[6] S. Yuan, X. Luo, H. L. Chan, C. Xiao, Y. Dai, M. Xie, J. Hao, *Nat. Commun.* **2019**, *10*, 1775.
[7] T. Lehnert, M. Ghorbani-Asl, J. Koester, Z. Lee, A. V. Krasheninnikov, U. Kaiser, *ACS Appl. Nano Mater.* **2019**, *2*, 3262.
[8] E. Wu, Y. Xie, J. Zhang, H. Zhang, X. Hu, J. Liu, C. Zhou, D. Zhang, *Sci. Adv.* **2019**, *5*, eaav3430.
[9] W. Wang, S. Kim, M. Liu, F. A. Cevallos, R. J. Cava, N. P. Ong, *Science* **2020**, *368*, 534.
[10] J. Chen, P. Li, J. Zhu, X. M. Wu, R. Liu, J. Wan, T. L. Ren, *IEEE Trans. Electron Devices* **2021**, *68*, 4748.
[11] W. Hou, A. Azizimanesh, A. Sewaket, T. Peña, C. Watson, M. Liu, H. Askari, S. M. Wu, *Nat. Nanotechnol.* **2019**, *14*, 668.
[12] M. J. Mleczko, A. C. Yu, C. M. Smyth, V. Chen, Y. C. Shin, S. Chatterjee, Y.-C. Tsai, Y. Nishi, R. M. Wallace, E. Pop, *Nano Lett.* **2019**, *19*, 6352.
[13] R. Ma, H. Zhang, Y. Yoo, Z. P. Degregorio, L. Jin, P. Golani, J. Ghasemi Azadani, T. Low, J. E. Johns, L. A. Bendersky, A. V. Davydov, S. J. Koester, *ACS Nano* **2019**, *13*, 8035.
[14] W. Zhou, X. Zou, S. Najmaei, Z. Liu, Y. Shi, J. Kong, J. Lou, P. M. Ajayan, B. I. Yakobson, J. C. Idrobo, *Nano Lett.* **2013**, *13*, 2615.
[15] H.-P. Komsa, S. Kurasch, O. Lehtinen, U. Kaiser, A. V. Krasheninnikov, *Phys. Rev. B* **2013**, *88*, 035301.
[16] Y. Yu, G. Wang, S. Qin, N. Wu, Z. Wang, K. He, X.-A. Zhang, *Carbon* **2017**, *115*, 526.
[17] O. Lehtinen, H. P. Komsa, A. Pulkin, M. B. Whitwick, M. W. Chen, T. Lehnert, M. J. Mohn, O. V. Yazyev, A. Kis, U. Kaiser, A. V. Krasheninnikov, *ACS Nano* **2015**, *9*, 3274.
[18] H. Liu, H. Zheng, F. Yang, L. Jiao, J. Chen, W. Ho, C. Gao, J. Jia, M. Xie, *ACS Nano* **2015**, *9*, 6619.

© 2024 The Authors. Small Structures published by Wiley-VCH GmbH

26884062, 2024, 7, Downloaded from https://onlinelibrary.wiley.com/doi/10.1002/sstr.202400027 by Xian Jiaotong University, Wiley Online Library on [19/12/2024]. See the Terms and Conditions (https://onlinelibrary.wiley.com/terms-and-conditions) on Wiley Online Library for rules of use; OA articles are governed by the applicable Creative Commons License

[19] H. Zhu, Q. Wang, L. Cheng, R. Addou, J. Kim, M. J. Kim, R. M. Wallace, *ACS Nano* **2017**, *11*, 11005.
[20] Q. Liang, Q. Zhang, X. Zhao, M. Liu, A. T. S. Wee, *ACS Nano* **2021**, *15*, 2165.
[21] P. Man, D. Srolovitz, J. Zhao, T. H. Ly, *Acc. Chem. Res.* **2021**, *54*, 4191.
[22] P. M. Coelho, H. P. Komsa, H. Coy Diaz, Y. Ma, A. V. Krasheninnikov, M. Batzill, *ACS Nano* **2018**, *12*, 3975.
[23] B. Wang, Y. Xia, J. Zhang, H.-P. Komsa, M. Xie, Y. Peng, C. Jin, *Nano Res.* **2020**, *13*, 1889.
[24] F. S. Ohuchi, B. A. Parkinson, K. Ueno, A. Koma, *J. Appl. Phys.* **1990**, *68*, 2168.
[25] B. A. Parkinson, F. S. Ohuchi, K. Ueno, A. Koma, *Appl. Phys. Lett.* **1991**, *58*, 472.
[26] H. Liu, L. Jiao, F. Yang, Y. Cai, X. Wu, W. Ho, C. Gao, J. Jia, N. Wang, H. Fan, W. Yao, M. Xie, *Phys. Rev. Lett.* **2014**, *113*, 066105.
[27] H. P. Komsa, A. V. Krasheninnikov, *Adv. Electron. Mater.* **2017**, *3*, 1600468.
[28] M. Batzill, *J. Phys.: Condens. Matter* **2018**, *30*, 493001.
[29] H. C. Diaz, Y. Ma, R. Chaghi, M. Batzill, *Appl. Phys. Lett.* **2016**, *108*, 191606.
[30] S. Barja, S. Wickenburg, Z.-F. Liu, Y. Zhang, H. Ryu, M. M. Ugeda, Z. Hussain, Z.-X. Shen, S.-K. Mo, E. Wong, M. B. Salmeron, F. Wang, M. F. Crommie, D. F. Ogletree, J. B. Neaton, A. Weber-Bargioni, *Nat. Phys.* **2016**, *12*, 751.
[31] L. Dong, G.-Y. Wang, Z. Zhu, C.-X. Zhao, X.-Y. Yang, A.-M. Li, J.-L. Chen, D.-D. Guan, Y.-Y. Li, H. Zheng, M.-H. Xie, J.-F. Jia, *Chin. Phys. Lett.* **2018**, *35*, 066801.
[32] Y. Ma, H. C. Diaz, J. Avila, C. Chen, V. Kalappattil, R. Das, M. H. Phan, T. Cadez, J. M. Carmelo, M. C. Asensio, M. Batzill, *Nat. Commun.* **2017**, *8*, 14231.
[33] M. K. Jana, A. Singh, A. Sampath, C. N. R. Rao, U. V. Waghmare, *Z. Anorg. Allg. Chem.* **2016**, *642*, 1386.
[34] M. W. Chen, D. Ovchinnikov, S. Lazar, M. Pizzochero, M. B. Whitwick, A. Surrente, M. Baranowski, O. L. Sanchez, P. Gillet, P. Plochocka, O. V. Yazyev, A. Kis, *ACS Nano* **2017**, *11*, 6355.
[35] J. Lin, S. T. Pantelides, W. Zhou, *ACS Nano* **2015**, *9*, 5189.
[36] Y. Ma, S. Kolekar, H. Coy Diaz, J. Aprojanz, I. Miccoli, C. Tegenkamp, M. Batzill, *ACS Nano* **2017**, *11*, 5130.
[37] H. Tian, Y. Ma, Z. Li, M. Cheng, S. Ning, E. Han, M. Xu, P. F. Zhang, K. Zhao, R. Li, Y. Zou, P. Liao, S. Yu, X. Li, J. Wang, S. Liu, Y. Li, X. Huang, Z. Yao, D. Ding, J. Guo, Y. Huang, J. Lu, Y. Han, Z. Wang, Z. G. Cheng, J. Liu, Z. Xu, K. Liu, P. Gao, et al., *Nature* **2023**, *615*, 56.
[38] L. Lichtenstein, C. Büchner, B. Yang, S. Shaikhutdinov, M. Heyde, M. Sierka, R. Włodarczyk, J. Sauer, H.-J. Freund, *Angew. Chem., Int. Ed.* **2012**, *51*, 404.
[39] P. Y. Huang, S. Kurasch, A. Srivastava, V. Skakalova, J. Kotakoski, A. V. Krasheninnikov, R. Hovden, Q. Mao, J. C. Meyer, J. Smet, D. A. Muller, U. Kaiser, *Nano Lett.* **2012**, *12*, 1081.
[40] N. R. Glavin, C. Muratore, M. L. Jespersen, J. Hu, P. T. Hagerty, A. M. Hilton, A. T. Blake, C. A. Grabowski, M. F. Durstock, M. E. McConney, D. M. Hilgefort, T. S. Fisher, A. A. Voevodin, *Adv. Funct. Mater.* **2016**, *26*, 2640.
[41] Z. Yang, J. Hao, S. P. Lau, *J. Appl. Phys.* **2020**, *127*, 220901.
[42] J. Zhang, Y. Xia, B. Wang, Y. Jin, H. Tian, W. K. Ho, H. Xu, C. Jin, M. Xie, *2D Mater.* **2021**, *8*, 015006.
[43] L. Lei, J. Dai, H. Dong, Y. Geng, F. Cao, C. Wang, R. Xu, F. Pang, Z.-X. Liu, F. Li, Z. Cheng, G. Wang, W. Ji, *Nat. Commun.* **2023**, *14*, 6320.
[44] S. M. Hus, R. Ge, P.-A. Chen, L. Liang, G. E. Donnelly, W. Ko, F. Huang, M.-H. Chiang, A.-P. Li, D. Akinwande, *Nat. Nanotechnol.* **2021**, *16*, 58.
[45] R. Ge, X. Wu, M. Kim, J. Shi, S. Sonde, L. Tao, Y. Zhang, J. C. Lee, D. Akinwande, *Nano Lett.* **2018**, *18*, 434.
[46] S. Manzeli, D. Ovchinnikov, D. Pasquier, O. V. Yazyev, A. Kis, *Nat. Rev. Mater.* **2017**, *2*, 17033.
[47] W. Li, X. Qian, J. Li, *Nat. Rev. Mater.* **2021**, *6*, 829.
[48] Y. Li, D. Wu, D. Wang, Y. Zhang, T. Min, Y. Pan, *Adv. Mater. Interfaces* **2023**, *10*, 2202043.
[49] Y. Pan, R. Guzman, S. Li, W. Xu, Y. Li, N. Tang, H. Yin, J. He, A. Wu, J. Chen, W. Zhou, X. Xu, Y. Ye, *Nat. Synth.* **2022**, *1*, 701.
[50] J. Park, K.-H. Xue, M. Mouis, F. Triozon, A. Cresti, *Phys. Rev. B* **2019**, *100*, 235403.
[51] P. Valerius, S. Kretschmer, B. V. Senkovskiy, S. Wu, J. Hall, A. Herman, N. Ehlen, M. Ghorbani-Asl, A. Grüneis, A. V. Krasheninnikov, T. Michely, *2D Mater.* **2020**, *7*, 025005.
[52] F. Ahmed, A. M. Shafi, D. M. A. Mackenzie, M. A. Qureshi, H. A. Fernandez, H. H. Yoon, M. G. Uddin, M. Kuittinen, Z. Sun, H. Lipsanen, *Adv. Mater. Interfaces* **2021**, *8*, 2100950.

© 2024 The Authors. Small Structures published by Wiley-VCH GmbH

26884062, 2024, 7, Downloaded from https://onlinelibrary.wiley.com/doi/10.1002/sstr.202400027 by Xian Jiaotong University, Wiley Online Library on [19/12/2024]. See the Terms and Conditions (https://onlinelibrary.wiley.com/terms-and-conditions) on Wiley Online Library for rules of use; OA articles are governed by the applicable Creative Commons License